

Numerical Methods in Magnetic Resonance Imaging: The Bloch-Torrey Equation

Jonathan Doucette^{a,b}

^a*UBC MRI Research Centre, University of British Columbia, 2221 Wesbrook Mall, Vancouver, BC, Canada.*

^b*Department of Physics and Astronomy, University of British Columbia, 6224 Agricultural Road, Vancouver, BC, Canada.*

April 12, 2018

In magnetic resonance imaging, insight into different imaging modalities can be gained through the simulation of the magnetic resonance signal measured by the scanner. This signal is modelled as a functional of the solution to the parabolic Bloch-Torrey partial differential equation. In this work, I compare various numerical techniques for solving the Bloch-Torrey equation in the presence of discontinuous data, with the goal of optimising the trade-off between solution accuracy and computation time.

Introduction

In magnetic resonance imaging (MRI), the magnetic resonance (MR) signal within a given region which is measured by an MRI scanner is directly proportional to the magnitude of the net magnetization vector \mathbf{M} within that region. In tissue, \mathbf{M} arises due to the superposition of the magnetic moments of water molecules, also known as *spins* in MRI nomenclature. Ordinarily, \mathbf{M} is zero in tissue, as spins are randomly oriented and therefore their vector sum is zero on the average. In MRI, however, there is a large and constant external magnetic field \mathbf{B}_0 which forces the alignment of the magnetized spins with \mathbf{B}_0 . This allows for the measurement, and importantly, the manipulation of the otherwise negligible net magnetization \mathbf{M} of the spins.

In one common type of MRI scan, a *gradient echo* scan, \mathbf{M} is initially flipped into the transverse plane through the application of a radio frequency (RF) magnetic pulse. Immediately, \mathbf{M} begins to realign with \mathbf{B}_0 exponentially quickly. The rate $R(\mathbf{x})$ at which this realignment occurs, however, depends on local tissue properties. Additionally, there is a characteristic precession of \mathbf{M} about \mathbf{B}_0 as it realigns. This precession occurs at a rate $\omega(\mathbf{x})$ which, too, depends on local tissue properties. Lastly, spins are free to diffuse within their environment while realigning, meaning they will see varying $R(\mathbf{x})$ and $\omega(\mathbf{x})$ as they move through the tissue.

The Bloch-Torrey equation

In the continuum limit, the net magnetization \mathbf{M} within a given region is modelled as a continuous vector field, and

the complex dynamics which follow the initial RF pulse can be beautifully modelled as solutions to a parabolic partial differential equation (PDE) called the Bloch-Torrey equation [1]:

$$\begin{cases} u_t = D\Delta u - Ru + \omega v \\ v_t = D\Delta v - Rv - \omega u \end{cases} \quad (1)$$

Here, u and v are the x - and y -components of the magnetization \mathbf{M} and D is the diffusion constant. For short simulation times, or *echo times*, T , the z -component of \mathbf{M} does not change appreciably, and we need only consider the transverse magnetization $\mathbf{M}_\perp = (u, v)$.

The transverse Bloch-Torrey equation (1) may be equivalently written as

$$\mathcal{M}_t = D\Delta \mathcal{M} - \Gamma \mathcal{M} \quad (2)$$

where $\mathcal{M} = u + iv$ is the complex magnetization and $\Gamma(\mathbf{x}) = R(\mathbf{x}) + i\omega(\mathbf{x})$ is the complex decay rate. This form is both notationally convenient and conceptually illustrative; now, realignment with \mathbf{B}_0 corresponds to the magnitude of the (complex) transverse magnetization \mathcal{M} decaying to zero, and the precession of \mathbf{M} about \mathbf{B}_0 corresponds to the rotation of \mathcal{M} about the origin in the complex plane.

Signal simulation

This work will compare three different methods of simulating the signal $S(T)$ measured by an MRI scanner at a time T following an initial RF pulse: finite differences, splitting methods, and finite element methods.

The MR signal $S(T)$ is given by

$$S(T) = \left\| \int_{\Omega} \mathbf{M}_\perp(T) \, d\mathbf{x} \right\| \quad (3)$$

where $\mathbf{M}_\perp(T)$ is computed by solving (1) or (2). The initial transverse magnetization $\mathbf{M}_\perp(t = 0)$ will be taken to be $[0, 1]^T$ without loss of generality.

Geometry

The transverse magnetization \mathbf{M}_\perp will be simulated within a cubic domain Ω of size $3 \times 3 \times 3 \text{ mm}^3$ with a single cylinder

e-mail: jdoucette@phas.ubc.ca

of a variable radius a in the centre of the domain, as pictured in Figure 1.

This geometry is chosen for two reasons. First, biologically it represents a single vessel present within a cubic imaging voxel. Second, there exists an exact solution for $\omega(\mathbf{x})$ given the magnetic susceptibility χ of the cylindrical blood vessel [2]. For a cylinder of radius a , we have that

$$\omega(\mathbf{x}) = \begin{cases} \frac{\chi\gamma B_0}{2} \sin^2 \theta \frac{a^2}{x^2+y^2} \frac{y^2-x^2}{x^2+y^2}, & \text{outside cylinder} \\ \frac{\chi\gamma B_0}{6} (3 \cos^2 \theta - 1), & \text{inside cylinder} \end{cases} \quad (4)$$

where θ is the angle between the cylinder axis and \mathbf{B}_0 , and the transverse coordinates x and y are measured with respect to the cylinder axis. Example cross sections of $\omega(\mathbf{x})$ for varying θ can be seen in Figure 1. Note that $\omega(\mathbf{x})$ is constant within the cylinder, and jumps discontinuously to an otherwise smooth function outside of the cylinder.

The transverse relaxation rate $R(\mathbf{x})$ is piecewise constant, taking separate values inside and outside of the cylinder:

$$R(\mathbf{x}) = \begin{cases} R_{\text{tissue}}, & \text{outside cylinder} \\ R_{\text{blood}}, & \text{inside cylinder}, \end{cases} \quad (5)$$

where $0 < R_{\text{tissue}} < R_{\text{blood}}$ are positive constants.

Properties of the Bloch-Torrey equation

Static solution

If $D = 0$, solutions to (2) are simply complex exponentials

$$\mathcal{M}(\mathbf{x}, t) = \mathcal{M}_0 e^{-\Gamma(\mathbf{x})t} = \left(e^{-R(\mathbf{x})t} |\mathcal{M}_0| \right) e^{i(\phi_0 - \omega(\mathbf{x})t)}, \quad (6)$$

where we have written $\mathcal{M}_0 = |\mathcal{M}_0| e^{i\phi_0}$ in polar form. Equivalently, the static solution may be written

$$\mathbf{M}_{\perp} = e^{-R(\mathbf{x})t} \|\mathbf{M}_{\perp 0}\| \begin{pmatrix} \cos(\phi_0 - \omega(\mathbf{x})t) \\ \sin(\phi_0 - \omega(\mathbf{x})t) \end{pmatrix}. \quad (7)$$

In this form, it is clear to see that the magnitude $|\mathcal{M}| = \|\mathbf{M}_{\perp}\|$ of the transverse magnetization is exponentially damped at rate $R(\mathbf{x})$ and that the initial phase ϕ_0 changes at the constant rate $\omega(\mathbf{x})$, which can be interpreted as the transverse magnetization rotating about \mathbf{B}_0 at a constant angular velocity at each point in space.

Relation to the reaction-diffusion equation

The two-component reaction-diffusion equation, which models for example how the concentrations u and v of two chemicals change over time within a medium, is given by

$$\begin{cases} u_t = D\Delta u + F(u, v) \\ v_t = D\Delta v + G(u, v) \end{cases} \quad (8)$$

where F and G govern local chemical reactions which may increase or decrease the concentrations u and v depending on whether they are being produced or consumed.

The reaction-diffusion equation (8) corresponds directly to the Bloch-Torrey equation in the case of linear reaction terms $F = -Ru + \omega v$ and $G = -Rv - \omega u$. In this interpretation, $R(\mathbf{x})$ represents the local rate at which u and v are reacted away into waste products, and $\omega(\mathbf{x})$ represents the local rate at which u reacts into v and vice versa.

Weak form

The coupled system of PDEs (1) can be written as

$$\begin{cases} \mathbf{u}_t = -A\mathbf{u} & \text{in } \Omega, \quad t > 0 \\ \mathbf{u} = \mathbf{g} & \text{in } \Omega, \quad t = 0 \end{cases} \quad (9)$$

where $\mathbf{u} = [u, v]^T$ and

$$A = \begin{pmatrix} -D\Delta + R & -\omega \\ \omega & -D\Delta + R \end{pmatrix}. \quad (10)$$

Now, consider the vector test function $\mathbf{v} = [w, z]^T$ where $w, z \in V = H^1$. Then, the weak form of (9) is given by

$$\langle \mathbf{v}, \mathbf{u}_t \rangle = -\langle \mathbf{v}, A\mathbf{u} \rangle, \quad \forall \mathbf{v} \in V \times V \quad (11)$$

where

$$\langle \mathbf{v}, A\mathbf{u} \rangle = \int_{\Omega} \{ -Dw\Delta u + Rwu - \omega wv - Dz\Delta v + Rzv + \omega zu \} dx.$$

Applying zero Neumann boundary conditions on the boundary $\partial\Omega$, this simplifies to

$$\langle \mathbf{v}, A\mathbf{u} \rangle = \int_{\Omega} D(\nabla w \cdot \nabla u + \nabla z \cdot \nabla v) + R(wu + zv) + \omega(zu - wv) dx. \quad (12)$$

Coercivity and local magnetization decay

The bilinear form $\langle \mathbf{v}, A\mathbf{u} \rangle$ is coercive, as

$$\begin{aligned} \langle \mathbf{u}, A\mathbf{u} \rangle &= \int_{\Omega} D(\|\nabla u\|^2 + \|\nabla v\|^2) + R(u^2 + v^2) dx \\ &\geq \left(\min_{\mathbf{x}} R(\mathbf{x}) \right) \|\mathbf{u}\|_{L^2}^2 \end{aligned} \quad (13)$$

with $\min_{\mathbf{x}} R(\mathbf{x}) = R_{\text{tissue}} > 0$. From this, it is then easy to show that the L^2 -norm of the solution decreases in time:

$$\langle \mathbf{u}, \mathbf{u}_t \rangle = \int_{\Omega} uu_t + vv_t dx = \frac{1}{2} \frac{\partial}{\partial t} \int_{\Omega} u^2 + v^2 dx = \frac{1}{2} \frac{\partial}{\partial t} \|\mathcal{M}\|_{L^2}^2,$$

and so, for non-zero \mathbf{u} , we have that

$$\frac{1}{2} \frac{\partial}{\partial t} \|\mathcal{M}(\mathbf{x}, t)\|_{L^2}^2 = \langle \mathbf{u}, \mathbf{u}_t \rangle = -\langle \mathbf{u}, A\mathbf{u} \rangle < 0$$

and therefore $\|\mathcal{M}\|_{L^2}^2$ decreases monotonically with time when starting from a non-zero \mathcal{M}_0 . Note that this does not

imply that $S(t)$ decreases monotonically as well, although it does of course go to zero in the limit as $t \rightarrow \infty$.

Uniqueness

Suppose for contradiction that \mathbf{u}_1 and \mathbf{u}_2 are different solutions to (9) zero Neumann boundary conditions on $\partial\Omega$.

Then, let $\mathbf{w} = \mathbf{u}_1 - \mathbf{u}_2$. By linearity, we have that \mathbf{w} solves

$$\begin{cases} \mathbf{w}_t = -A\mathbf{w} & \text{in } \Omega, \quad t > 0 \\ \mathbf{w} = \mathbf{0} & \text{in } \Omega, \quad t = 0. \end{cases}$$

Now, we have that $\|\mathbf{w}(t=0)\|_{L^2} = 0$, and since we have shown that $\|\mathbf{u}\|_{L^2}$ is non-increasing for all solutions \mathbf{u} to (9), it must be that $\|\mathbf{w}\|_{L^2} \equiv 0$ for all time and therefore \mathbf{u}_1 must equal \mathbf{u}_2 almost everywhere for all time, a contradiction.

Existence and continuous dependence on data

Existence and continuous dependence on data of (weak) solutions to the Bloch-Torrey equation (1) follows directly from the analogy with the linear reaction-diffusion equations (8). Such results are greatly detailed in many texts, such as for example [3] and [4], and I will not go into further details here, except to say that (1) is indeed well posed with Neumann boundary conditions on $\partial\Omega$.

Methods

Finite difference methods

The simplest method for solving equation (2) is through a simple application of the method of lines to discretise the negative Laplacian $-\Delta$ using standard second order consistent centred differences, resulting in $-\Delta^h$ such that

$$-\Delta^h \mathcal{M}(\mathbf{x}_i) = \frac{6\mathcal{M}(\mathbf{x}_i) - \sum_{j \in \mathcal{J}_i} \mathcal{M}(\mathbf{x}_j)}{h^2} + \mathcal{O}(h^2) \quad (14)$$

where h is the uniform grid spacing and the sum is over the six neighbours of \mathbf{x}_i indexed by \mathcal{J}_i . It should be noted that this second order consistency will not actually be observed in practice, as due to the discontinuities in $R(\mathbf{x})$ and $\omega(\mathbf{x})$ we expect that the solution may have jumps in the gradient on the cylinder boundary.

Boundary conditions are taken to be periodic on the boundaries of the unit cube [5], as opposed to Neumann boundary conditions on the boundary of the cube and cylinder. This is due to simplicity of implementation and the inherent limitations of finite differences methods on irregular domains.

Γ is discretised to the diagonal matrix operator Γ^h such that $\Gamma_{ii}^h = \Gamma(\mathbf{x}_i)$, where \mathbf{x}_i is a point on the discretised grid.

What results is the discrete system

$$\frac{\partial}{\partial t} \mathcal{M}^h(t) = -A^h \mathcal{M}^h(t) \quad (15)$$

$$\Rightarrow \mathcal{M}^h(t) = e^{-A^h t} \mathcal{M}^h(0), \quad (16)$$

where $A^h = -D\Delta^h + \Gamma^h$ and the notation $e^{-A^h t}$ represents the *matrix exponential* [6] of the matrix $-A^h t$. In our case, although $A^h \in \mathbb{C}^{N^3 \times N^3}$ where N may be large, we need only compute the matrix exponential vector product – also known as the *action* of the matrix exponential – and not $e^{-A^h t}$ itself, which is in general full despite A^h being sparse [6]. Algorithms for computing the action of the matrix exponential are known [7, 8]. I use the algorithm described by Higham et al. in [9], as well as their MATLAB code *expmv*.

Note that although the periodic Laplacian operator Δ^h is singular due to the fact that the constant solution has eigenvalue zero, adding Γ^h shifts the positive constant diagonal $6/h^2$ up by $R(\mathbf{x}_i) + i\omega(\mathbf{x}_i)$, thereby making the matrix A^h strongly diagonally dominant and therefore non-singular by the Gershgorin circle theorem [10]. Therefore, the solution (16) to the system (15) exists and is unique.

The resulting signal $S^h(T)$ is computed by integrating the discrete solution $\mathcal{M}^h(T) = e^{-A^h T} \mathcal{M}_0^h$ using the trapezoidal rule and taking the absolute value of the result.

Operator splitting methods

Operator splitting methods for parabolic PDEs are useful when a differential operator has no closed form operator exponential, but can be split into a sum of operators which do. The operator exponential is the formal equivalent of the matrix exponential for differential operators, namely it is the operator defined such that $\mathbf{u}(\mathbf{x}, t) = e^{-At} \mathbf{u}_0(\mathbf{x})$ when $\partial_t \mathbf{u}(\mathbf{x}) = -A\mathbf{u}(\mathbf{x})$ with $\mathbf{u}_0(\mathbf{x})$ given.

Suppose a differential operator $A = T + V$ is given such that the action of the operator exponential $e^{-At} \mathbf{u}$ has no closed form, but the actions $e^{-Tt} \mathbf{u}$ and $e^{-Vt} \mathbf{u}$ do. Then, one can use *Strang splitting* [11, 12] to approximate the action of the operator exponential of A with that of T and V :

$$e^{-A\delta t} = e^{-(T+V)\delta t} \quad (17)$$

$$= e^{-T\delta t} e^{-V\delta t} + \mathcal{O}(\delta t^2) \quad (18)$$

$$= e^{-V\delta t/2} e^{-T\delta t} e^{-V\delta t/2} + \mathcal{O}(\delta t^3) \quad (19)$$

where the approximation errors are incurred due to the fact that T and V are assumed to not commute, i.e. $T(V\mathbf{u}) \neq V(T\mathbf{u})$. Were they to commute, both of these approximations would be exact.

In our case, from equation (2) we may take $A = T + V$ where $T = -D\Delta$ with periodic boundary conditions, and $V = \Gamma$. Then, the action of the evolution operators $e^{Dt\Delta}$ and $e^{-\Gamma t}$

in approximations (18) and (19) are known [13]:

$$e^{Dt\Delta}\mathcal{M}_0(\mathbf{x}) = \Phi(\mathbf{x}, t) * \mathcal{M}_0(\mathbf{x}) \quad (20)$$

$$e^{-\Gamma t}\mathcal{M}_0(\mathbf{x}) = e^{-\Gamma(\mathbf{x})t}\mathcal{M}_0(\mathbf{x}), \quad (21)$$

where $\Phi(\mathbf{x}, t)$ is the Gaussian kernel defined as

$$\Phi(\mathbf{x}, t) := \frac{1}{(4\pi Dt)^{3/2}} e^{-\mathbf{x}^2/4Dt} \quad (22)$$

and $*$ denotes the convolution over space. Note that, as opposed to the solution (16), the solution (20) and (21) is extremely fast to compute. The convolution in equation (20) can be computed efficiently using the Fast Fourier Transform (FFT), since the boundary conditions are periodic, and equation (21) only involves exponentiation and multiplication.

The resulting signal $S^h(T)$, as in the case of the finite differences, is computed by integrating the resulting discrete solution $M^h(T)$ using the trapezoidal rule and taking the absolute value of the result.

Finite element methods

The weak form (23) of the Bloch-Torrey equation is discretised using the method of lines and linear finite elements to obtain

$$\langle \mathbf{v}^h, \mathbf{u}_t^h \rangle = -\langle \mathbf{v}^h, A^h \mathbf{u}^h \rangle, \quad \forall \mathbf{v}^h \in V^h \times V^h \quad (23)$$

where $V^h \subset V = H^1$ is the space of linear finite elements on $\Omega^h \subset \Omega$. Note that Ω^h is only a proper subset of Ω when the cylinder interior is included in the domain. Otherwise, the discretisation is non-conforming.

Writing $\mathbf{u}^h = \begin{pmatrix} u^h \\ v^h \end{pmatrix}$ with u^h, v^h the vectors of nodal values of each PDE, the resulting linear system is

$$M^h \mathbf{u}_t^h = -A^h \mathbf{u}^h \quad (24)$$

where

$$\begin{aligned} A^h &= DK^h + R^h + W^h \\ M^h &= \begin{pmatrix} m^h & 0 \\ 0 & m^h \end{pmatrix} \quad K^h = \begin{pmatrix} k^h & 0 \\ 0 & k^h \end{pmatrix} \\ R^h &= \begin{pmatrix} r^h & 0 \\ 0 & r^h \end{pmatrix} \quad W^h = \begin{pmatrix} 0 & -w^h \\ w^h & 0 \end{pmatrix} \end{aligned}$$

where m^h and k^h are the usual mass and stiffness matrices for each of the coupled PDEs, and

$$r_{ij}^h := \int_{\Omega} R \phi_i \phi_j dx, \quad w_{ij}^h := \int_{\Omega} \omega \phi_i \phi_j dx.$$

Since $R(\mathbf{x})$ is strictly positive, r^h is symmetric positive definite as

$$\begin{aligned} (\mathbf{u}^h)^T r^h \mathbf{u}^h &= \sum_{i,j} \mathbf{u}_i^h \left(\int_{\Omega} R \phi_i \phi_j dx \right) \mathbf{u}_j^h \\ &= \int_{\Omega} R (\sum_i \mathbf{u}_i^h \phi_i)^2 dx \geq 0. \end{aligned}$$

Although w^h is not positive definite and A^h is not symmetric, A^h is still positive definite in the sense that

$$(\mathbf{u}^h)^T A^h \mathbf{u}^h = D(\mathbf{u}^h)^T K^h \mathbf{u}^h + (\mathbf{u}^h)^T R^h \mathbf{u}^h \geq 0$$

by the positive definiteness of K^h and R^h . This is the analogous property to the coercivity of $\langle \mathbf{u}, A\mathbf{u} \rangle$ in the weak form (13).

Time stepping for finite element methods

Asymmetric positive definite matrices do not in general have real eigenvalues. However the real part of their eigenvalues are all strictly positive. Therefore, time stepping methods for the system (24) should be chosen to be at least strongly A -stable so that iterates of the numerical solution decay at an exponential rate. The two time stepping methods which will be implemented are the L -stable backward Euler scheme and the A -stable TRBDF-2 method with parameter $\alpha = 2 - \sqrt{2}$. Additionally, the backward Euler scheme was chosen for its simplicity of implementation, and the TRBDF-2 method was chosen for its second order accuracy in time.

Backward Euler method: discretising the system (24) in time with the backward Euler method results in the time stepping iteration

$$(M^h + \delta t A^h) \mathbf{u}_+ = M^h \mathbf{u}_0 \quad (25)$$

TRBDF-2 method: discretising the system (24) in time with the TRBDF-2 method with parameter $\alpha = 2 - \sqrt{2}$ results in the time stepping scheme

$$(M^h + c_0 \delta t A^h) \mathbf{u}_\alpha = M^h \mathbf{u}_0 - c_0 \delta t A^h \mathbf{u}_0 \quad (26)$$

$$(M^h + c_0 \delta t A^h) \mathbf{u}_+ = c_+ M^h \mathbf{u}_\alpha + c_- M^h \mathbf{u}_0 \quad (27)$$

where $c_0 = 1 - 1/\sqrt{2}$, $c_\pm = (1 \pm \sqrt{2})/2$.

For both time stepping methods, the resulting signal $S^h(T)$ is computed by integrating the final discrete x - and y -solution components $u^h(T)$ and $v^h(T)$ and taking the magnitude of the resulting vector $S^h(T) = \|[S_x^h(T), S_y^h(T)]^T\|$.

Adaptive finite elements for the backward Euler method

For the backward Euler method, I will employ a simple *a posteriori* error estimate for the y -component of the signal $S_y(T)$ in order to create error indicators $\eta_{\mathcal{T}}$ on each tetrahedron \mathcal{T} for use in adaptive finite elements. This simple estimate will consider only errors due to the time stepping scheme, and not errors due to the discretisation itself. The y -component is used as opposed to the full signal due to the fact that $S(T)$ is a non-linear functional of the solution, whereas $S_y(T)$ is a linear functional. Moreover, since we take $(u_0, v_0) = (0, 1)$, in practice the magnitude of $S_y(T)$ remains much larger than that of $S_x(T)$ for the simulation

time T , and so the error in $S_y(T)$ is a good estimate for the error in $S(T)$.

Consider the linear system of ODEs

$$\begin{cases} u_t = Bu & \text{for } 0 < t \leq T \\ u(0) = u_0 \end{cases} \quad (28)$$

and the corresponding time-reversed dual problem

$$\begin{cases} -\phi_t = B^T \phi & \text{for } 0 \leq t < T \\ \phi(T) = \phi_0, \end{cases} \quad (29)$$

and suppose we are interested in bounding the error of a quantity of interest Q which is a linear functional of the solution at time T , taking the form

$$Q(T) = \psi \cdot u(T)$$

where ψ is a known constant vector.

Then, let equation (28) be solved using the backward Euler method, with unequal time steps allowed, and discretise u in time using the dG(0) discontinuous Galerkin method of order zero, which results in the discrete solution u^h being left-continuous piecewise constant on each time interval $(t_{n-1}, t_n]$.

Defining $e(T) = Q(T) - Q^h(T)$, it is shown in Section 4 of [14] that if ϕ_0 is set to equal ψ then

$$|e(T) \cdot \psi| \leq E_u \int_0^T \|\phi_t\| dt \leq E_u \sqrt{T \int_0^T \|\phi_t\|^2 dt} \quad (30)$$

where the second inequality follows from the Cauchy-Schwarz inequality and $E_u := \max_n \|u^h(t_n) - u^h(t_{n-1})\|$. Note also that $\phi_t = -B^T \phi$ may be used in computing the time integral of $\|\phi_t\|$.

The integral over $\|\phi_t\|^2$ may be split into a sum of integrals over the components $(\phi_t)_i^2$; define the root mean square of the derivative components $q_i := \sqrt{\frac{1}{T} \int_0^T (\phi_t)_i^2 dt}$. Then, identifying the nodal values q_i with an appropriately defined interpolated function $q(\mathbf{x})$, the error indicator $\eta_{\mathcal{T}}$ is chosen to be

$$\eta_{\mathcal{T}} = \frac{1}{|\mathcal{T}|} \int_{\mathcal{T}} E_u T q(\mathbf{x}) dx. \quad (31)$$

In order to use this estimate for the weak form of the Bloch-Torrey equation (24) with the goal of estimating the error in $Q(T) = S_y(T)$, $\psi = \mathbf{w}_{v^h}$ is set to be the vector of quadrature weights for the numerical integration of the y -component v^h of \mathbf{u}^h , and B is set to $-(M^h)^{-1}A^h$.

Then, the change of variables $\phi = M^h \Phi$ results in the time-reversed dual problem

$$\begin{cases} -M^h \Phi_t = -(A^h)^T \Phi & \text{for } 0 \leq t < T \\ \Phi(T) = (M^h)^{-1} \mathbf{w}_{v^h} \end{cases} \quad (32)$$

which may be solved using any time stepping method. Note additionally that $\phi_t = M^h \Phi_t = (A^h)^T \Phi$ is still inexpensive to compute.

Numerical experiments

Gold standard solution

As the Bloch-Torrey equation has no closed form solution, even for this simple geometry, the solution signal $S(T)$ which will be used for comparison will simply be the finite element solution computed from the system (24) on a fine mesh of approximately 250^3 degrees of freedom and small time steps of 0.125 ms until the final simulation time of 40 ms. In fact, two different gold standard signals $S(T)$ will be computed: first, with the cylinder interior excluded from the domain and Neumann boundary conditions imposed on the cylinder wall, $S_{\text{HOLLOW}}(T)$; second, with the interior of the cylinder included in the domain and no boundary conditions imposed on the cylinder wall, $S_{\text{UNION}}(T)$.

Finite differences vs. finite elements

Four methods of solving the Bloch-Torrey PDE will be investigated in this experiment. For finite differences, the Strang splitting method (19) and the exponential matrix method (16) in conjunction with Higham's *expmv* integrator [9] will be performed. For finite element methods, time stepping of the weak form (24) with both the backward Euler method (25) and the TRBDF-2 method (26) / (27) will be performed. The total simulation time for all simulations is chosen to be $T = 40$ ms, a typical echo time for a gradient echo MRI scan. The direct solution via *expmv* was computed to machine precision in time for grid sizes ranging from $50 \times 50 \times 50$ to $250 \times 250 \times 250$. Time steps were varied from 8 ms down to 0.25 ms, in powers of two, for both the splitting method and the finite element methods. A uniform grid of $250 \times 250 \times 250$ elements is used for finite differences, and a mesh with approximately 250^3 degrees of freedom was used for the finite element methods. The interior of the cylinder was included in this experiment, and no boundary conditions were imposed on the cylinder walls. The gold standard value S_{UNION} is used for calculating error values.

Boundary conditions on the cylinder

In this experiment, the affect of including the interior of the cylinder in Ω and not applying boundary conditions on the wall will be compared with excluding the interior of the cylinder, and applying zero Neumann boundary conditions on the cylinder wall. The missing signal from the interior of the domain is corrected for analytically in order to compare with the interior included case: since $R(\mathbf{x})$ and $\omega(\mathbf{x})$ are both constant within the cylinder walls, and because the interior of the domain is separated from the exterior with reflective Neumann boundary conditions, \mathcal{M} is given simply by the static solution (6) on the interior of the cylinder. The analytically corrected $S_{\text{HOLLOW}}(T)$ gold standard signal is used for error computations.

Adaptive finite element methods

In this experiment, the efficiency of the finite element method with adaptive mesh refinement is investigated. The interior of the cylinder is excluded from the domain, and zero Neumann boundary conditions are imposed on the cylinder wall. Time stepping for both the forward and dual problems is performed with either the backward Euler method (25) or the TRBDF-2 method (26)/ (27). Note that the *a posteriori* error estimate (30) was derived assuming backward Euler time stepping; nevertheless, the error indicators η_T will be tested using the TRBDF-2 method, as well. The non-adaptive time stepping will use a fixed mesh with approximately 250^3 degrees of freedom; time steps will vary from 8 ms down to 0.25 ms. The adaptive mesh refinement will use a time step of 1 ms and an initial mesh with approximately 10^3 degrees of freedoms, with four subsequent mesh refinements performed in which the cells in the top 1/3 of error values, as indicated by η_T , will be refined. The gold standard value $S_{\text{HOLLOW}}(T)$ is used for error computations.

Results and discussion

Boundary conditions: The root mean square (RMS) distance travelled by a freely diffusing particle in n -dimensions is $d_{\text{RMS}} = \sqrt{2nDT}$ [15]. With $T = 40$ ms and diffusion constant $D = 3.037 \mu\text{m}^2/\text{ms}$ [16], the mean free diffusion distance in $n = 3$ dimensions is $d_{\text{RMS}} = 27.0 \mu\text{m}$. When compared to the $3 \text{ mm} = 3000 \mu\text{m}$ edge length of the cubic domain Ω and the $250 \mu\text{m}$ radius of the cylinder, it is apparent that diffusing spins do not travel far on the average.

Intuitively, then, periodic vs. Neumann boundary conditions on the boundary of the cubic domain Ω should have little effect on the resulting signal $S(T)$ due to the relatively small volume boundary volume within the RMS diffusion distance of particles within the domain. Additionally, a diffusing particle being reflected off of the boundary could similarly be interpreted as a particle from the other side of the domain diffusing into the region. So, as long $R(\mathbf{x})$ and $\omega(\mathbf{x})$ do not change significantly from one boundary edge to the other, the effect of the choice of boundary condition should be minimal.

This intuition is verified in Figure 2. The finite difference methods converge to a signal $S(T)$ which is within a fraction of a percent from that of the finite element solution.

Now, this argument does not directly apply to the cylinder boundary, where $R(\mathbf{x})$ and $\omega(\mathbf{x})$ vary discontinuously. In this case, unless the vessel is sufficiently small so as to have minimal contribution to the total signal, one should expect that the Neumann boundary conditions on the cylinder wall in the FEM case vs. no boundary conditions applied in the finite differences case should have a non-negligible effect.

However, Figure 3 shows otherwise. Indeed, whether or not the cylinder boundary is included in the domain, the finite element methods converge to effectively the same value. This effect is likely due to the small diffusion distance, as well, as in the limit that $D \rightarrow 0$ both topologies will converge to the static solution on the whole domain. Therefore, with sufficiently small d_{RMS} , it is reasonable to expect that differences in signal will become negligible.

Speed, and adaptive finite elements: The aim of this study is to determine the optimal trade-off between accuracy and speed for the Bloch-Torrey equation. In comparing the powerful but expensive finite element methods with the straightforward but limited finite difference method, the only manner in which finite element methods might keep up with finite difference methods is through the use of a considerably smaller number of degrees of freedom in computing the signal $S(T)$.

In comparing Figures 2 and 5, it appears that adaptive finite element methods can in fact compete with finite difference methods. The effect of the error indicators η_T can be seen in Figure 4.

Generation of meshes with finite element methods was much slower in these experiments, however, and was not including the timing. Therefore, if the meshes need to be simulated often enough, finite difference methods may still be considerably less expensive.

Conclusion and future work

Finite difference methods have been compared and contrasted with finite element methods for their use in solving the Bloch-Torrey equation. I have shown that the powerful and flexible framework of finite element methods need not necessarily sacrifice speed, particularly when the quantity of interest is a linear functional of the partial differential equation solution, when compared to finite difference methods.

Adaptive finite elements, through the use of a simple *a posteriori* error estimate, allowed for a drastic decrease in the required number of degrees of freedom for computing the signal $S(T)$ resulting from the finite element solution to the Bloch-Torrey equation, leading to solution speeds which are competitive with finite difference methods.

There is still much improvement to be made, however. In this simple method, discretisation error was not considered in the *a posteriori* bound. Additionally, as $R(\mathbf{x})$ and $\omega(\mathbf{x})$ are discontinuous at the cylinder boundary, a more sophisticated finite element basis – such as discontinuous Galerkin finite elements – would be more suitable for this problem. Lastly, geometry generation was limited to a simple cylinder. In practical simulations with tissue compartment boundaries and other domain discontinuities, geometry generation is significantly more complex.

References

- [1] H. C. Torrey, “Bloch Equations with Diffusion Terms,” *Phys. Rev.*, vol. 104, pp. 563–565, Nov. 1956.
- [2] Y.-C. N. Cheng, J. Neelavalli, and E. M. Haacke, “Limitations of Calculating Field Distributions and Magnetic Susceptibilities in MRI using a Fourier Based Method,” *Phys Med Biol*, vol. 54, pp. 1169–1189, Mar. 2009.
- [3] C. Kuttler, “Reaction-diffusion equations with applications,” in *Internet Seminar*, 2011.
- [4] W. Liu, *Elementary Feedback Stabilization of the Linear Reaction-Convection-Diffusion Equation and the Wave Equation*. Springer Science & Business Media, Dec. 2009. Google-Books-ID: YobRZn1HLhYC.
- [5] D. V. Nguyen, J.-R. Li, D. Grebenkov, and D. Le Bihan, “A finite elements method to solve the Bloch–Torrey equation applied to diffusion magnetic resonance imaging,” *Journal of Computational Physics*, vol. 263, pp. 283–302, Apr. 2014.
- [6] C. Moler and C. Van Loan, “Nineteen Dubious Ways to Compute the Exponential of a Matrix,” *SIAM Rev.*, vol. 20, pp. 801–836, Oct. 1978.
- [7] M. Caliari, P. Kandol, A. Ostermann, and S. Rainer, *Comparison of various methods for computing the action of the matrix exponential*. submitted.
- [8] C. Moler and C. Van Loan, “Nineteen Dubious Ways to Compute the Exponential of a Matrix, Twenty-Five Years Later,” *SIAM Rev.*, vol. 45, pp. 3–49, Jan. 2003.
- [9] A. Al-Mohy and N. Higham, “Computing the Action of the Matrix Exponential, with an Application to Exponential Integrators,” *SIAM J. Sci. Comput.*, vol. 33, pp. 488–511, Jan. 2011.
- [10] S. Gerschgorin, “über die abgrenzung der eigenwerte einer matrix,” *Bulletin de l’Académie des Sciences de l’URSS. Classe des sciences mathématiques et na*, vol. 6, pp. 749–754, 1931.
- [11] G. Strang, “On the Construction and Comparison of Difference Schemes,” *SIAM J. Numer. Anal.*, vol. 5, pp. 506–517, Sept. 1968.
- [12] S. MacNamara and G. Strang, “Operator Splitting,” in *Splitting Methods in Communication, Imaging, Science, and Engineering*, Scientific Computation, pp. 95–114, Springer, Cham, 2016.
- [13] R. Guardiola, “Monte carlo methods in quantum many-body theories,” in *Microscopic Quantum Many-Body Theories and Their Applications*, Lecture Notes in Physics, pp. 269–336, Springer, Berlin, Heidelberg, 1998. DOI: 10.1007/BFb0104529.
- [14] Eriksson K., Johnson C., and Logg A., “Adaptive Computational Methods for Parabolic Problems,” *Encyclopedia of Computational Mechanics*, Nov. 2004.
- [15] T. S. Ursell, “The Diffusion Equation A Multi-dimensional Tutorial,” *California Institute of Technology, Pasadena, Tech. Rep*, 2007.
- [16] M. Holz, S. R. Heil, and A. Sacco, “Temperature-dependent self-diffusion coefficients of water and six selected molecular liquids for calibration in accurate 1h NMR PFG measurements,” *Phys. Chem. Chem. Phys.*, vol. 2, pp. 4740–4742, Jan. 2000.

Figures and Tables

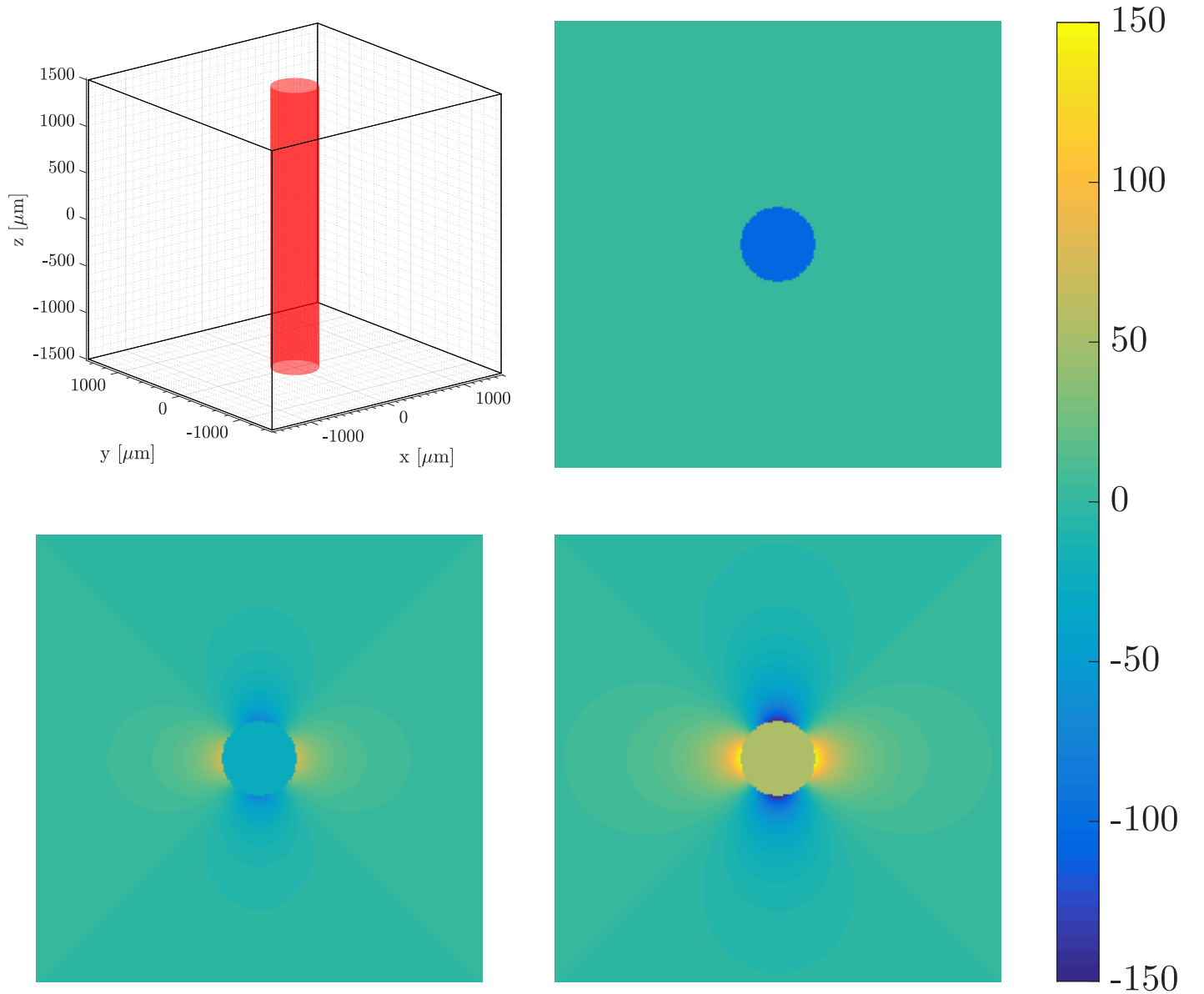


Figure 1: The top-left figure shows the geometry of the domain Ω . The $3 \times 3 \times 3 \text{ mm}^3$ cubic domain is populated with a single cylinder – representing a cerebral blood vessel – parallel to the z -direction. The radius of the cylinder is $250 \mu\text{m}$. The frequency map $\omega(\mathbf{x})$ generated by this configuration is computed according to equation (4). Example cross-sections in the z -direction of $\omega(\mathbf{x})$ are shown for $\theta = 0^\circ$, (top right), 45° (bottom left), and 90° (bottom right). All simulations in this study were performed with $\theta = 90^\circ$. It can be easily observed that the magnitude of $\omega(\mathbf{x})$ is largest near the cylinder wall, decays to zero far from the cylinder axis, and is constant within the cylinder.

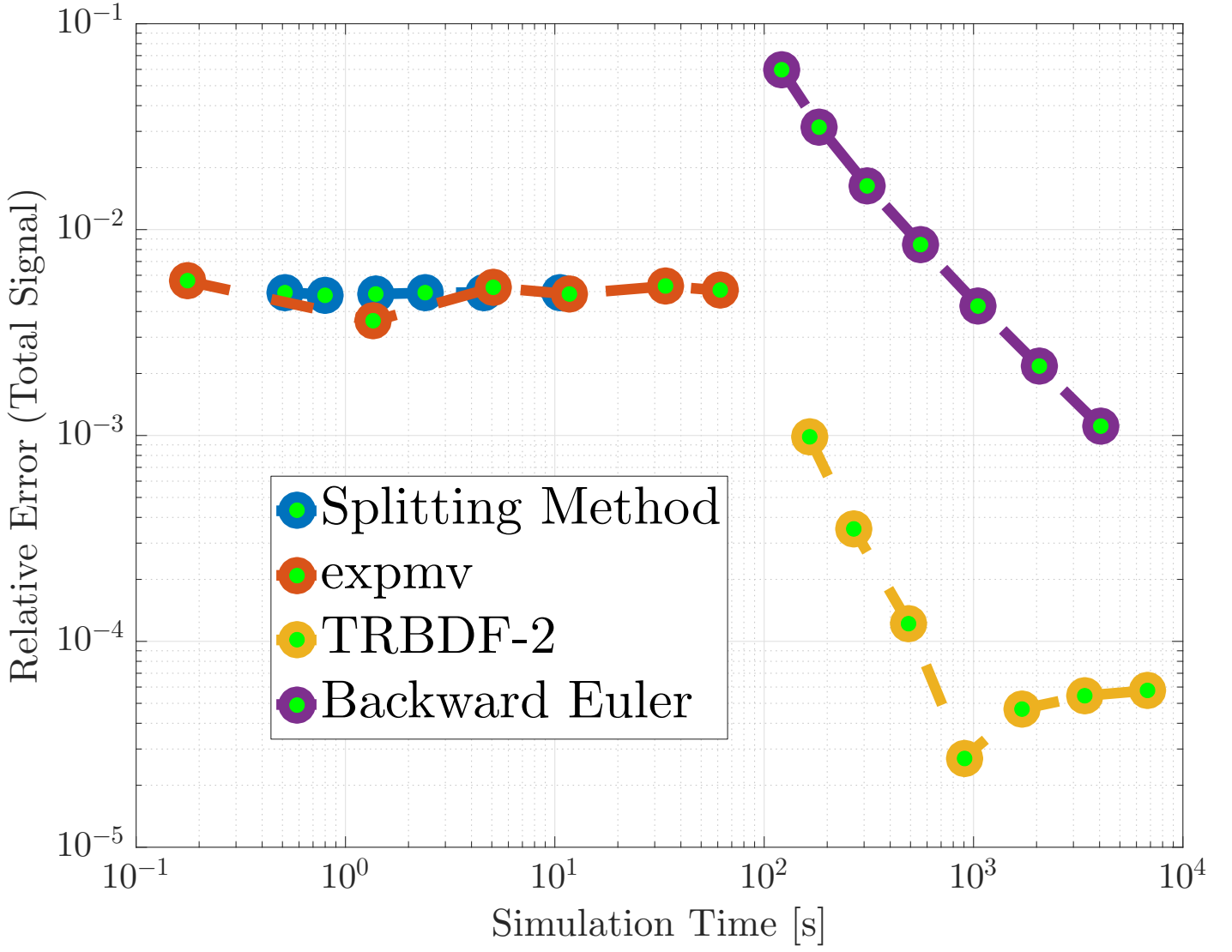


Figure 2: Comparison between solving the Bloch-Torrey equation with four methods: finite differences with the Strang splitting method (19), finite differences with the exponential matrix method (16) in conjunction with Higham’s *expmv* integrator [9], and finite element methods with the interior of the cylinder included in the domain, time stepping with both the backward Euler method (25) and the TRBDF-2 method (26)/ (27). The total simulation time was $T = 40$ ms. Time steps were varied from 8 ms down to 0.25 ms for the splitting method and the FEM time stepping methods, with grid sizes of $250 \times 250 \times 250$ for the finite difference methods, and approximately the same number of degrees of freedom for the FEM methods. The direct solution via *expmv* was computed to machine precision for grid sizes ranging from $50 \times 50 \times 50$ to $250 \times 250 \times 250$.

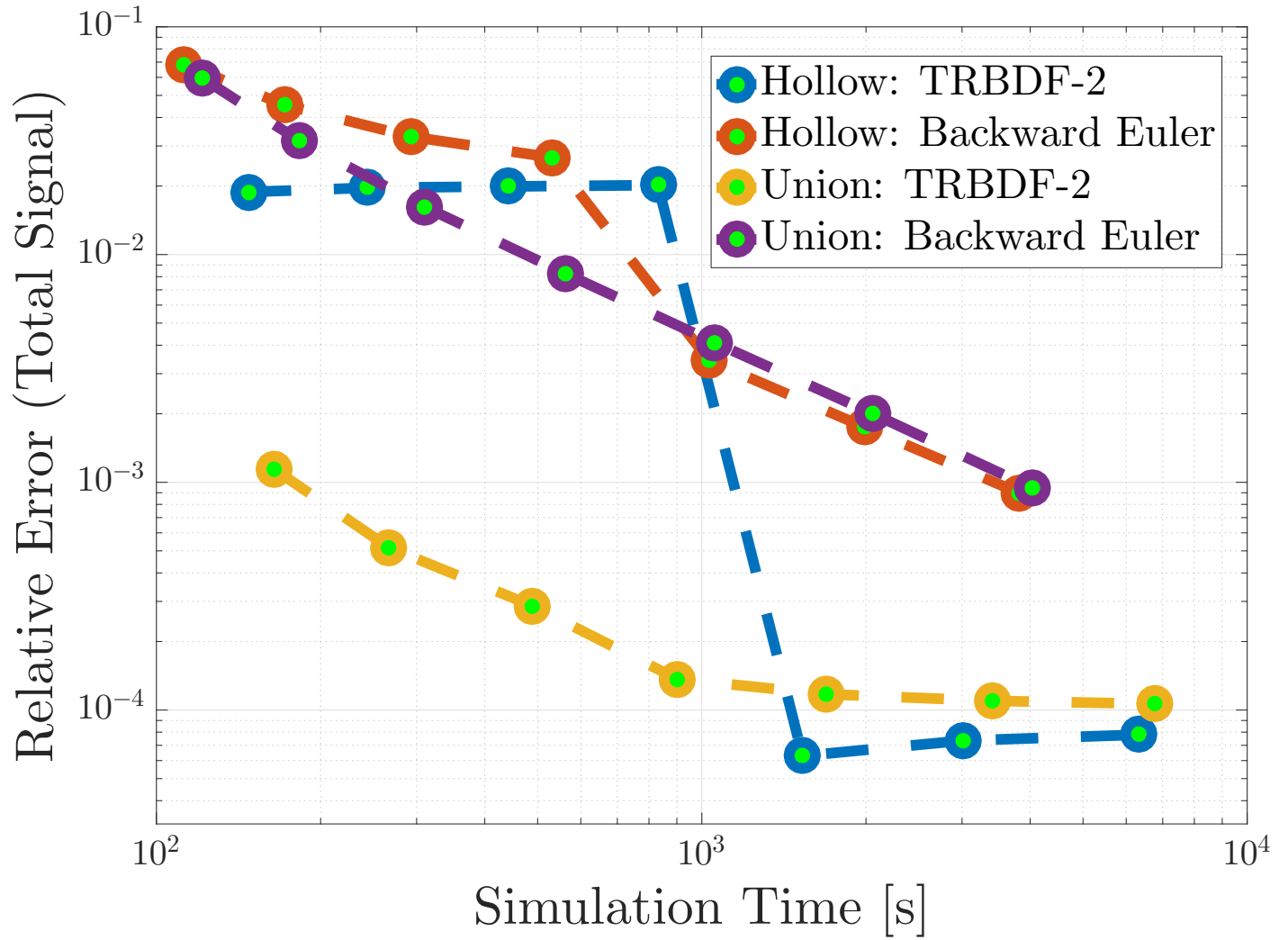


Figure 3: Comparison between including and excluding the interior of the cylinder in the domain Ω when solving the Bloch-Torrey equation with FEM, time stepping with both the backward Euler method (25) and the TRBDF-2 method (26)/ (27). The missing signal from the interior of the domain is corrected for analytically; $R(\mathbf{x})$ and $\omega(\mathbf{x})$ are both constant within the cylinder walls, and so \mathcal{M} is given simply by the static solution (6). Interestingly, the Neumann boundary conditions on the cylinder walls appear to have little effect on the total signal.

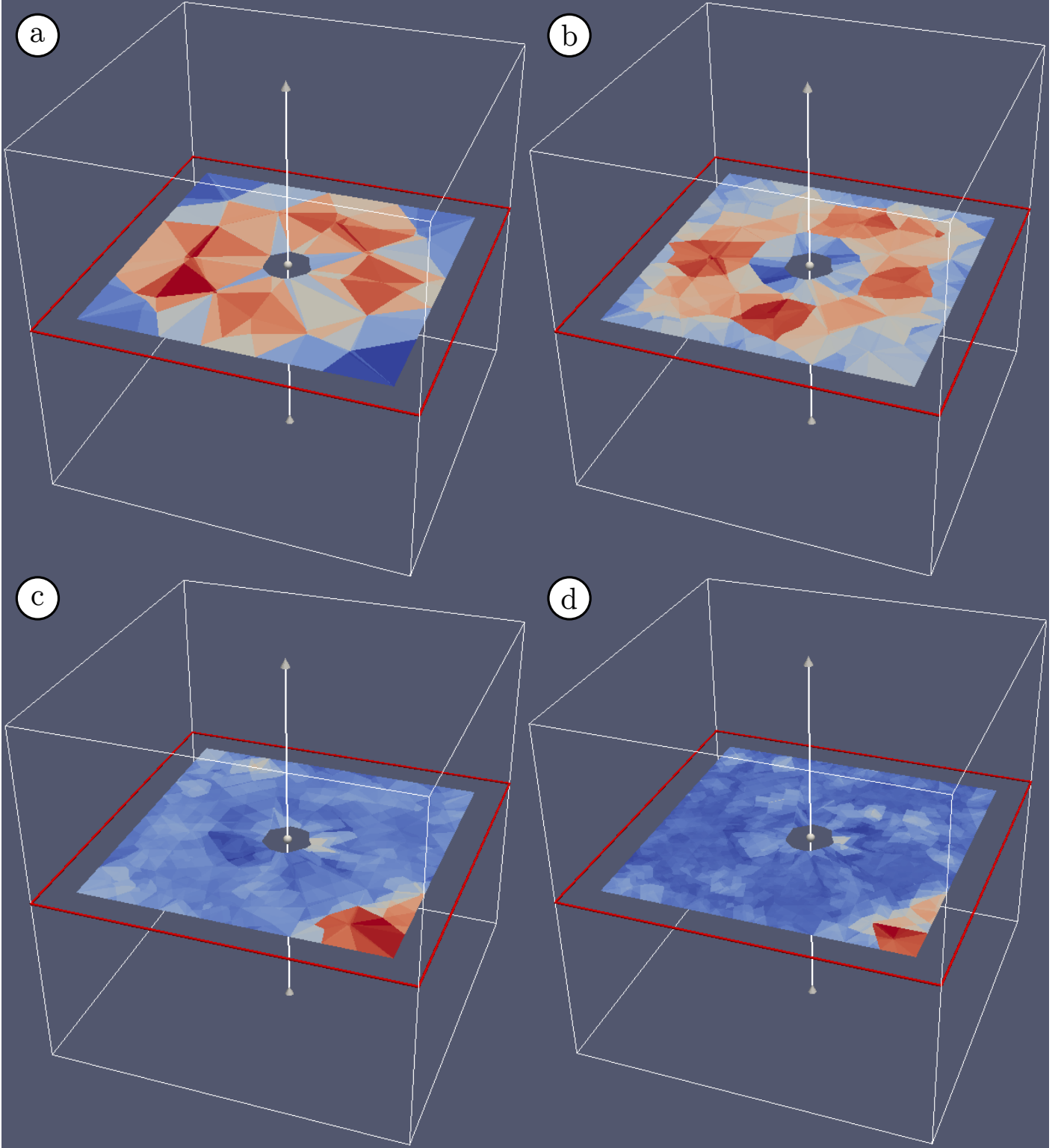


Figure 4: Example cross sections of the indicator functions $\eta_{\mathcal{T}}$ from equation (31) formed when solving the Bloch-Torrey equation with FEM and adaptive mesh refinement. The mesh is iteratively refined three times, starting with the mesh (a) with approximately 10^3 degrees of freedom, through to mesh (d). The interior of the cylinder was excluded from the domain, and time stepping for the forward and dual problems was performed using the backward Euler method (25). It can be seen that initially, the mesh is refined nearest to the cylinder wall. The final mesh is more refined in the interior compared to the exterior, as may be expected. Additionally, (c) and (d) show that large tetrahedra at the boundary are eventually refined, too.

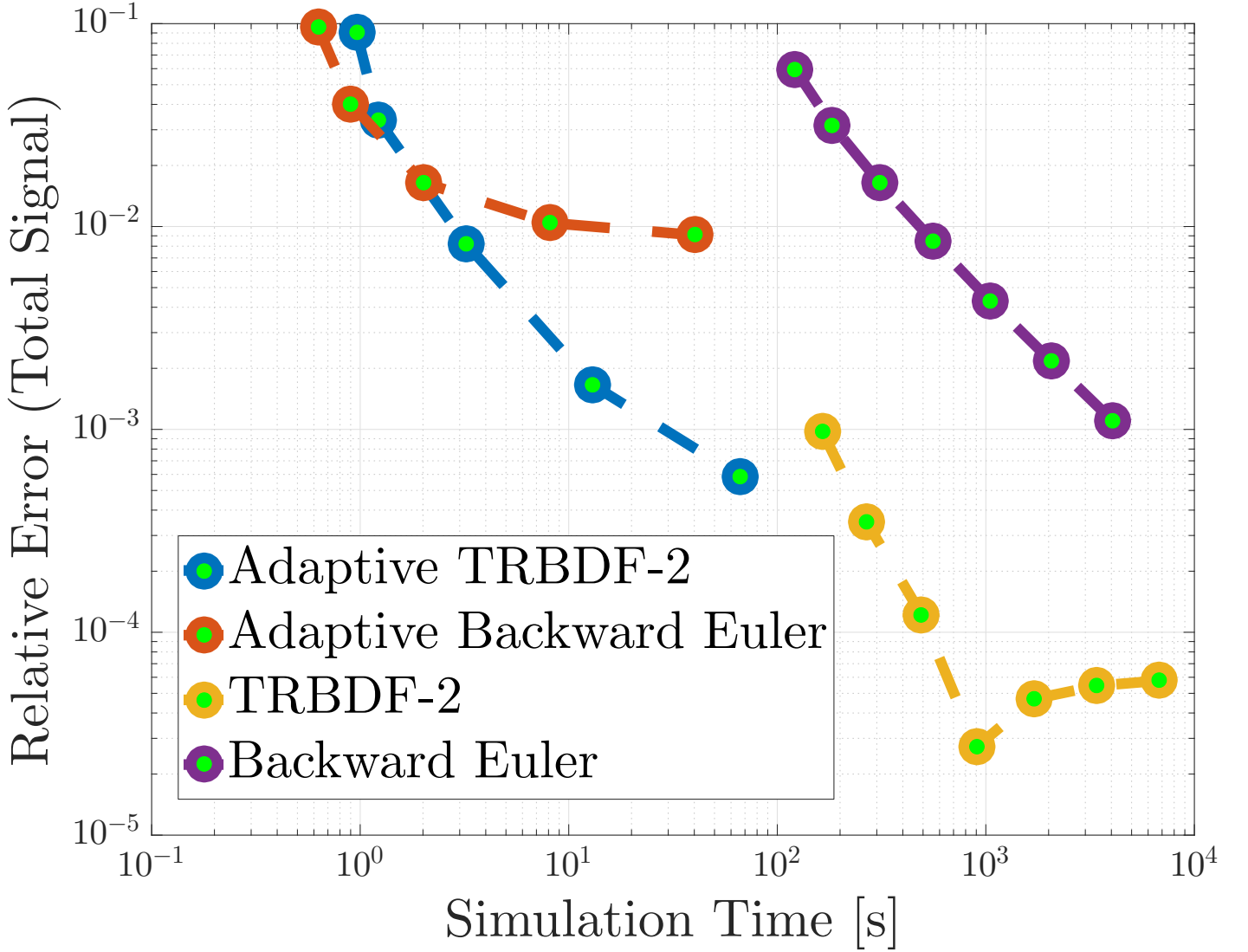


Figure 5: Comparison between adaptive mesh refinement and fixed mesh solving of the Bloch-Torrey equation using FEM. The interior of the cylinder was excluded from the domain, and time stepping for the forward and dual problems was performed with either the backward Euler method (25) or the TRBDF-2 method (26)/ (27). The total simulation time was $T = 40$ ms. The non-adaptive time stepping used a fixed mesh with approximately 250^3 degrees of freedom; time steps were varied from 8 ms down to 0.25 ms. The adaptive mesh refinement used a time step of 1 ms and an initial mesh with approximately 10^3 degrees of freedoms. Four mesh refinements were performed, refining the top 1/3 of cells as indicated by η_T each iteration. Note that the *a posteriori* error estimate (30) was derived assuming backward Euler time stepping; nevertheless, the error indicators η_T performed well empirically for the TRBDF-2 method, as well.